UNIVERSITÀ DEGLI STUDI DI PADOVA

Dipartimento di Fisica e Astronomia "Galileo Galilei"

Corso di Laurea in Fisica

Tesi di Laurea

Time resolution measurements of SpaCal prototype for LHCb upgrade 2

Relatore

Prof. Donatella Lucchesi

Correlatore

Dr. Lorenzo Sestini

Dr. Davide Zuliani

Laureando

Lisa Arnone

Anno Accademico 2021/2022

Contents

Introduction

This thesis work aims to inquire about a future Upgrade of LHCb, one of the Large Hadron Collider (LHC) experiments at CERN. The goal is to study the possibility to introduce time measurement in the Electromagnetic Calorimeter. Specifically, it aims to study the time performance of two prototypes: a Spaghetti Calorimeter (SpaCal), made of tungsten and GAGG cristal fibers (SpaCal W/GAGG) and a SpaCal made of tungsten and polysterene fibers (SpaCal W/Polystyrene). Analysed data have been collected during the test-beam campaign in August 2021 at the Super Proton Syncrothron (SPS) at CERN.

The thesis is structured in the following way:

1. Chapter 1: a brief description of the LHC accelerator complex and the LHCb experiment is presented, particularly showing for the latter its main features and purposes;
2. Chapter 2: in this chapter, the High Luminosity LHC (HL-LHC) program is described and the plans for the LHCb Upgrade (referred as LHCb Upgrade phase II) are discussed. Particularly, an accurate description of the Electromagnetic Calorimeter (ECAL) and the future developments for the Upgrade II phase are presented. The focus will be on the description of the prototypes currently under study and the motivations to upgrade the actual ECAL;
3. Chapter 3: this chapter is devoted to the analysis of the data taken during the test-beam campaign in August 2021. Two main studies are presented: the measurement of the time resolution as function of the beam particles energy, and the measurement of the time resolution as a function of the region hit by the incident beam particles. Both analyses have been performed on SpaCal W/GAGG and SpaCal W/Polystyrene prototypes data;
4. Chapter 4: conclusions on the analysis results are presented, with some observations for future test-beams.

Chapter 1

LHCb description

1.1 LHC overview

The LHC [1] is the world biggest particle accelerator, with a circumference of 26.7 km. Operating since 2008. It was built in 10 years in the previous site of the Large Electron-Positron (LEP) collider experiment at around 100 m underground, placed at the border between France and Switzerland, near Geneve.

The LHC structure consists in two vacuum pipes in which proton beams are accelerated in opposite directions. The two pipes have long straight sections equipped with radio-frequency (RF) cavities kept in cryomodules to preserve their electromagnetic field. These RF cavities are meant to accelerate the particles with an oscillating field at a certain frequency. In this way the beam is kept at a fixed energy by finely tuning the frequency so that particles are always accelerated. Inside the pipes almost 1.5×10^{11} protons are gathered in 2808 bunches of around 30 cm long, spaced by 25 ns which make a non-continuous beam bent by superconducting magnets kept at 1.9 K using liquid helium and which reach a dipolar field above 8.3 T. Before entering the pipes, protons have to be accelerated in several steps following the chain Linac2 - Proton Synchrotron Booster (PSB) - Proton Synchrotron (PS) - Super Proton Synchrotron (SPS) to reach the required energy. In the last accelerator ring, the protons exiting from SPS reach an energy of 450 GeV and this allows them to be accelerated in the last stage (LHC) to have at present a centre of mass energy of 13 TeV. In the next runs LHC will reach the nominal energy of 14 TeV per collision.

The two vacuum pipes cross each other in four interaction points, where the main experiments are located: CMS (Compact Muon Solenoid), ATLAS (A Toroidal LHC ApparatuS), ALICE (A Lead Ion Collision Experiment) and LHCb. The proton bunches collide in these points and the particles generated from these collisions are detected by the experiments. A variable strongly correlated with the collision cross section σ is the luminosity L, defined by the following equation

$$N = L\sigma \tag{1.1}$$

where N is the number of events per second generated by the collisions. The LHC nominal peak luminosity is $L = 2 \cdot 10^{34}$ cm^{2}s^{-1}.

1.2 LHCb detector

LHCb [2] is an experiment originally designed to study b and c hadrons in the forward region of the proton-proton collisions.

The detector apparatus is a single arm spectrometer with an angular coverage from 10 to 300 mrad. It weights around 5600 ton, it is 21 m long, 10 m high and 13 m wide and it is located at the LHC interaction point called Point 8. It extends longitudinally along the beam direction - which is chosen

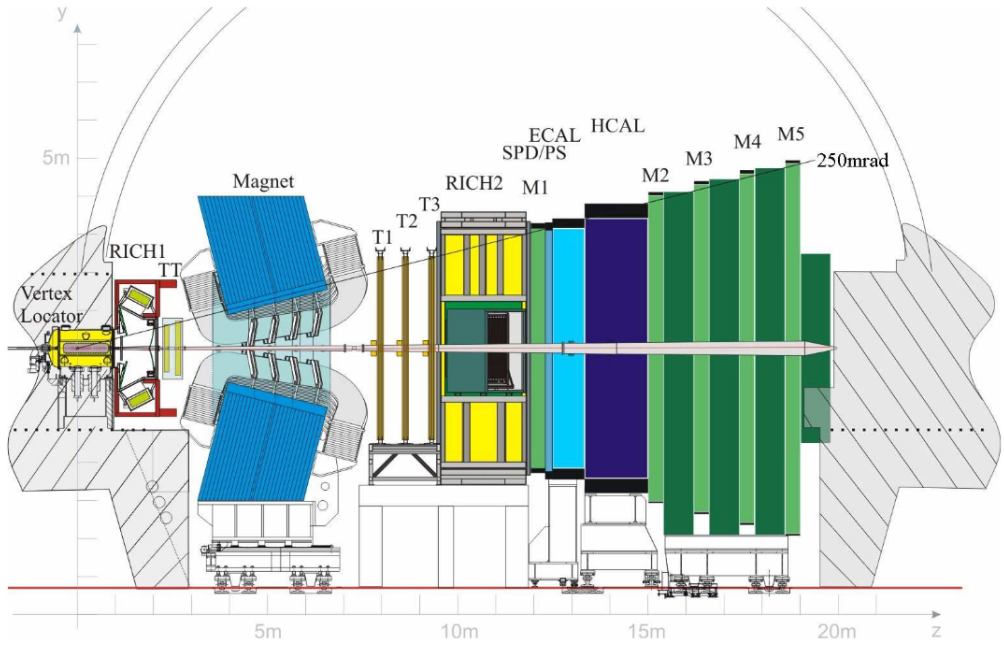

Figure 1.1: Section of the LHCb detector in yz plane [2].

to be the z axis in a cartesian reference system, as shown in figure (1.1). In this reference system the y axis is parallel and opposite to the gravity, while the x axis is chosen to form right-handed coordinates.

LHCb is equipped with a tracking system and a particle identification system (PID). The former is composed by the Vertex Locator and four tracking stations. The latter includes two Cherenkov detectors, the calorimeter system (electromagnetic and hadronic calorimeters), and finally the muon chambers.

At LHCb the nominal LHC instantaneous luminosity is reduced with a levelling technique [10], in order to achieve cleaner events with an average number of proton-proton collision per bunch-crossing (pile-up, defined as the mean number of interactions in visible events/bunch crossing) around 1 in the data taking period between 2010 and 2018. A lower luminosity is adequate to do all the measurements dealt by LHCb such as the b quark production which has a sufficiently high cross section to be investigated at this luminosity.

1.2.1 Vertex Locator (VELO)

The VErtex LOcator (VELO) is a very crucial part of the detection process because it allows to locate production and decay vertices of b and c hadrons. This is necessary to provide accurate measurements for what concerns particle lifetimes, but also to identify primary and secondary vertices, fundamental for identifying the heavy flavour hadrons (flavour tagging).

The VELO is located close to the interaction region and it is a tracker formed by a series of 42 silicon modules which provide particles polar coordinates (r, ϕ), where r is the radial distance from the beam line and ϕ is the azimuthal angle. The sensors are placed at a given radial distance from the beam and they are grouped into two halves which can be moved remotely along the x axis, as shown in figure 1.2 to fit the needed aperture for LHC beam injection. The r sensor measures the radial coordinate from 8 mm to 42 mm while the ϕ sensor has an angular acceptance range from 15 mrad to 390 mrad. The sensors are kept in vacuum at $-5\ ^{\circ}C$ to limit radiation damage. Thanks to the precise alignment of the VELO, a spatial resolution around 7 μm on the x and y coordinates is obtained.

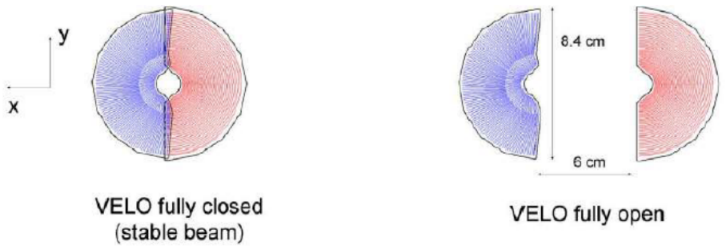

Figure 1.2: Cross section of VELO sensor closed configuration (left) and open configuration (right) [2].

1.2.2 Cherenkov detectors (RICH)

In order to identify particles such as pions or kaons produced by the collision, there are two modules of Ring Imaging CHerenkov detectors (RICH1 and RICH2) placed in two different z positions because of the different momentum range close to or far from the collision point. RICH1 is placed immediately after the VELO and is responsible for the detection of low momentum particles (with $p \sim 1-60\ GeV/c$) in a wide angular acceptance range (almost all the LHCb acceptance range) while RICH2 is placed after the tracking modules and detects higher momenta ($p \sim 15 - 100\ GeV/c$) with a limited angular acceptance $< 120\ mrad$. Both the detectors have a combination of spherical and flat mirrors to focus the Cherenkov light and convey it to Hybrid Photon Detectors (HPD) which convert photons into electrons.

1.2.3 Magnet

Another important aspect is the measurement of particles momentum, thanks to the estimation of their curvature radius due to the Lorentz force, as described by the relation

$$p = qrB \tag{1.2}$$

where p and q are respectively the momentum and the charge of the particle, while r is the curvature radius due to the effect of the magnetic field B. This can be done with a dipolar magnetic field in the y direction created by a magnet placed between the Trigger Tracking module and the tracking stations. This magnet is a (warm) conductor of 1600 ton of weight structured with Aluminium conical coils placed symmetrically in the magnet yoke. Their shape is such as to create two slopes to cover all the detector acceptance. The bending power of the magnet ($\int B \cdot dl$) is 4 $T \cdot m$. The magnetic field direction can be inverted changing the current direction which generates it in order to correct for detector mis-alignments.

1.2.4 Tracking system

Together with the VELO there are four planar tracking modules, the Tracking Turicensis (TT), placed after RICH1, and three tracking stations T1, T2 and T3 located between the magnet and RICH2.

Depending on the distance from the beam, two different technologies are used: the Inner Trackers (IT) made of silicon microstrips closer to the beam pipe while the Outer Trackers (OT) are straw-tubes employed in the outer region. This division is shown in the figure 1.3 where it can be noticed that the first module TT (smaller then the other three and closer to the beam) covers all the acceptance range of LHCb. The other three modules are made as the TT in the central part and in the outer part from an array of straw tubes modules, each formed by drift tubes containing a gas mixture to have a better drifting resolution.

1.2.5 Calorimeters

The calorimeter system is fundamental for measuring particles energy and for the particle identification. As for other LHC experiments, the calorimeter system is made by an Electromagnetic Calorimeter (ECAL) and a Hadronic Calorimeter (HCAL). The structure and functioning of the current ECAL

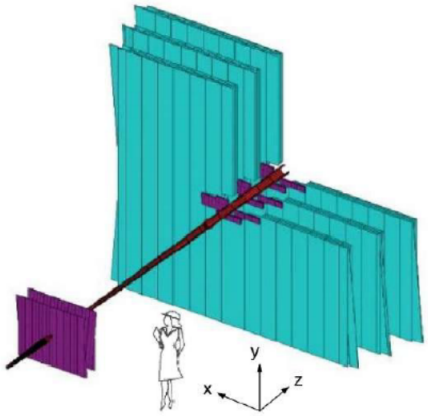

Figure 1.3: Schematic view of the tracking stations TT and T1,2,3, with the IT (violet) and the OT (green) [2].

is fundamental for this thesis, since the future ECAL upgrade and its performance are discussed in the next Chapters.

ECAL is placed at 12.5 m from the interaction point and its acceptance covers all the LHCb one. The particles measured by ECAL are photons and electrons. Before entering ECAL, particles interact with the Scintillating Pad Detector/Preshower (SPD/PS) system: electrons are detected by the SPD, while photons interact both with SPD and PS thanks to a 15 mm (which corresponds to $2.5\chi_0$ radiation length) lead layer between those two. Hadrons are not detected by the SPD/PS system.

The ECAL uses the photons and electrons interactions with matter such as pair production and bremsstrahlung to absorb and convert photons in signals proportional to the absorbed energy. The scintillation signal is then conveyed into wavelenght-shifting (WSL) fibers and read by photomultipliers tubes (PMT). ECAL is made of 12.12×12.12 cm^2 modules divided in cells of different sizes, depending on the region: these modules are formed by 9, 4 or 1 cell per module and respectively are placed in the inner, middle and outer part of the ECAL, as shown in figure 1.4. The technology of the cells is the Shashlik [7], i.e. sampling scintillator/lead structure readout by plastic WLS fibres. The overall module consists in a 42 cm stack ($25X_0$, where X_0 is the radiation length) formed by alternate 66 Pb and scintillator Polystyrene layers respectively 2 mm and 4 mm thick.

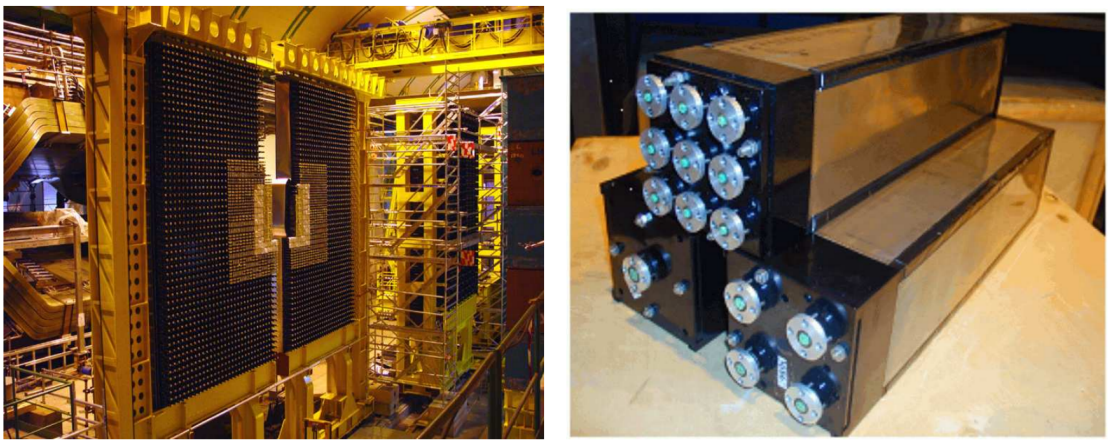

Figure 1.4: Downstream view of the ECAL with the two halves open where the 3 regions can be seen (left). The ECAL modules with Shashlik technology with 9, 4, 1 cell per module (right) [2].

This technology was chosen because it was a good compromise between good energy resolution (1.3), fast time response and acceptable radiation resistance.

The ECAL energy resolution is

$$\left(\frac{\sigma_E}{E}\right)_{ECAL} = \frac{10\%}{\sqrt{E}} \oplus 1\% \tag{1.3}$$

where E is the particle energy in GeV, $\oplus$ indicates the quadratic sum of the two terms and the term on the right is given by structural imperfections in calorimeter construction.

Considering HCAL, its structure is very similar to the ECAL one, it is placed at 13.33 m distance from the interaction point and is made by alternating layers of 1 cm of iron and scintillation material (again mainly Polystyrene) for 5.6 radiation lengths. Here charged or neutral hadrons deposit their remaining energy which is converted into signal passing through WSL plastic fibers and PMTs. The energy resolution is worse than the ECAL one as it can be seen in the following equation:

$$\left(\frac{\sigma_E}{E}\right)_{HCAL} = \frac{69\%}{\sqrt{E}} \oplus 9\% \tag{1.4}$$

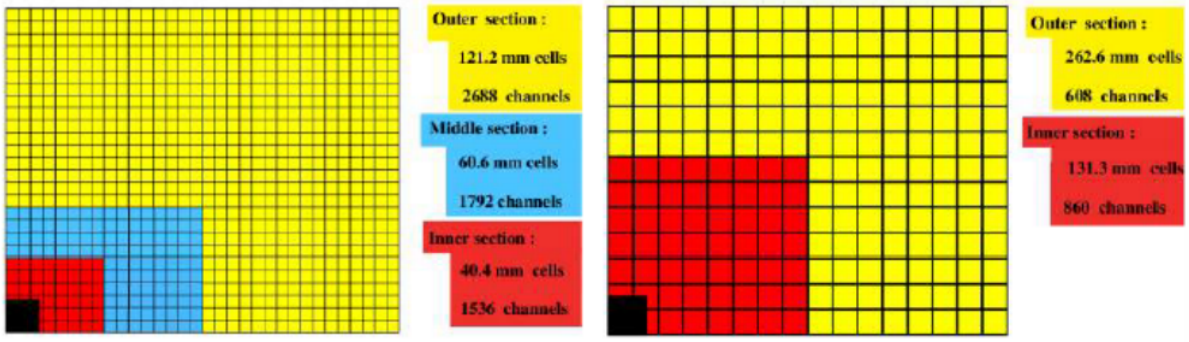

Figure 1.5: Inner, middle and outer part of the suddivision with their respective module and cell number for ECAL (left) and HCAL (right) [2].

1.2.6 Muon chambers

In the outer part of the LHCb detector there are five muon detection station (M1-M5) with rectangular shape on the plane perpendicular to the beam axis and whose surface increases with the distance from the interaction point. The first chamber is placed just after RICH2 and functions as a trigger and with M2 and M3 constitutes the tracks identifying chambers with a resolution of few millimetres. M4 and M5 instead have a limited spatial resolution and therefore are meant to simply identify the penetrating particles. These modules are made of 80 cm thick iron absorbers, corresponding to $\sim 20\chi_0$ (absorbing length), which allow to detect muons with momentum greater than 6 GeV/c [8].

1.2.7 Physics measurements with ECAL

The goal of this thesis is to discuss the upgrade of the LHCb electromagnetic calorimeter, therefore in this section physics measurements where ECAL plays a crucial role are briefly presented:

- jets: the fragmentation of gluons and quarks produce streams of particles called jets. They are fundamental for measuring the $Z \to b\bar{b}$ production, and in the search for the $H \to c\bar{c}$ decay, that is one of the most important goals of future LHCb upgrades. ECAL is used to measure the electromagnetic component of hadronic jets, contributing in determining the jet energy scale and resolution;
- precision electroweak measurements: the measurement of W and Z boson properties is important for the precise determination of Standard Model parameters, like the W boson mass and the electroweak mixing angle. The reconstruction of $W \to e\nu$ and $Z \to ee$ decay channels can be performed by identifying the high energy electrons with ECAL, that is also used to correct the electron momentum for bremsstrahlung losses;

- lepton flavour violation: b hadrons can decay with electrons or muons in the final state. The branching ratios of these two different types of decay, as well as their angular properties, can be compared to search for possible violation of the lepton flavour universality principle. Therefore the electron identification performed by ECAL is fundamental in this kind of measurements;
- b-hadron radiative decays: ECAL is also used to measure the energy of photons and π^0 produced in the radiative decays of b hadrons. At LHCb these decay channels are used to measure the parameters of the CP violation in b-hadron decays, like the γ angle of the CKM matrix.

Chapter 2

Upgrades and calorimeter

2.1 The High Luminosity program

In order to investigate rare processes and so the evidence of new physics beyond the Standard Model, the number of data gathered from interactions should be increased, and with that the luminosity whence the High Luminosity program for LHC (HL-LHC). To give an example, it is expected that LHC will be able to detect 15 million Higgs bosons per year, while in 2017 they were around three million [5].

To achieve almost 10 times the current integrated luminosity, it is necessary to make some changes not only to the LHC machine but also to the detectors, that in order to keep a good resolution should be equipped with better or even new components.

For what concerns the LHC machine, from 2018 the civil engineering work has been started at Point 1 (the CMS site) and it proceeded during the long shutdown period LS2 (2018-2021) and will continue on LS3 (2025-2027) following the schedule shown in figure 2.1 which will be better explained in the next section. The parts which will be improved are, for instance, the magnets: in fact, because of the higher number of collisions, the particle beam has to be more focused and intense and this will be obtained with new superconducting quadrupole magnets. Their material, a compound of Niobium (Nb) and Tin (Sn), is new in the accelerator technology field and will allow to reach a magnetic field of 12 T as opposed to the current one of 8 T. Together with these magnets come new 'crab cavities', whose task is to tilt the beam increasing the collision area. Last, there are improved dipole magnets, superconducting links, collimators and a new injector chain with a new linear accelerator Lineac4.

2.2 LHCb upgrades

The new integrated luminosity shall be obtained gradually. It is expected to increase slightly until 2030 and then rise greatly. Of course major changes are done during the long shutdown periods but some modifications or adaptations are done in course. As mentioned before, with the HL-LHC changes on the LHC machine, the detectors too have to adapt. For the purpose of this thesis, LHCb upgrades are explained in more detail, especially the ones that affect the calorimeter system. It is possible to identify the schedule of LHCb activity with respect to the luminosity profile in figure 2.1 [7].

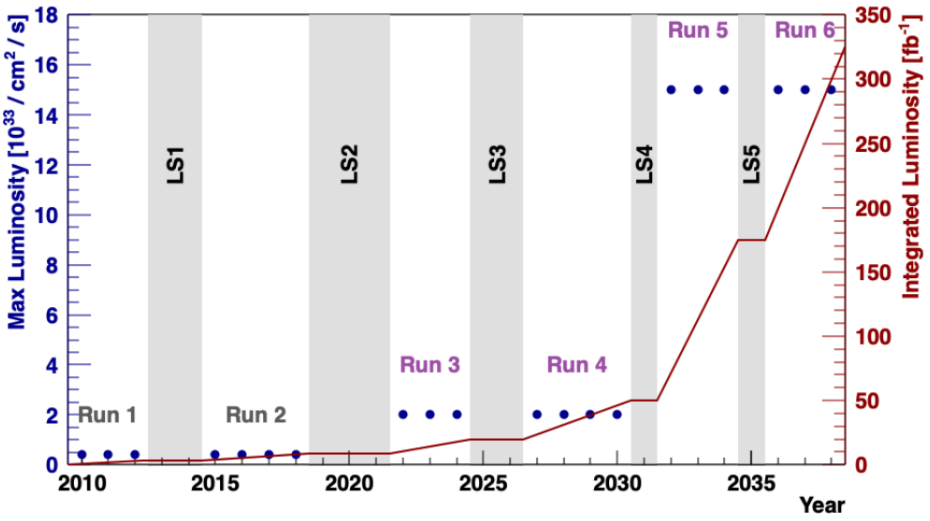

Figure 2.1: Schedule of LHCb Upgrade I (Run 3 and 4) and Upgrade II (Run 5 and 6) in the LHC program context from 2008 to 2038 with the respective integrated Luminosity profile [5].

Upgrade I corresponds to Run 3 and 4 and Upgrade II would be Run 5 and 6. The dots indicate the instantaneous luminosity reached while the line is the integrated luminosity. At the end of the HL-LHC phase LHCb is expected to collect almost 300 fb^{-1} of data.

One totally new requirement will be the possibility to have time-precision measurements in different components of the detector in order to be able to correctly identify the particles interaction vertices and therefore suppress combinatorial background. In fact, as well as the luminosity, also the pile-up will increase, making the process of identifying primary vertices more difficult. The average pile-up (*i.e.* hard interaction per bunch crossing) expected in Run 3 and 4 is around 10. In Run 5 and 6 is expected that the pile-up will be > 40 producing around 2000 charged particles within the LHCb acceptance at luminosity $1.5 \cdot 10^{34}\ cm^2 s^{-1}$, as opposed to the current value of one. Consequently the distance between two primary vertices will become 1.5 mm instead of 4.2 mm of Upgrade I. For this reason, it will be necessary to implement new technologies, especially in the PID-involved sub-detectors namely RICH, ECAL but also VELO. In addition to that, the new components shall be resistant to radiation damage due to the increased particles number.

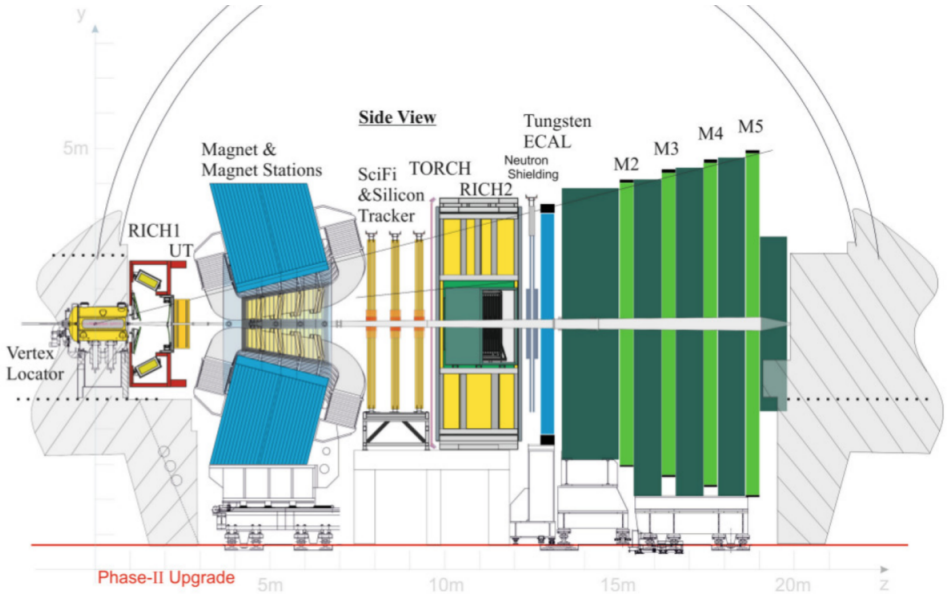

Figure 2.2: Schematic view of LHCb detector at the end of the Upgrade II [5].

As it can be seen in figure 2.2 there are few changes in the spectrometer structure and in its components arrangement.

- VELO will be changed already in Upgrade I and then improved in Upgrade II. The (r, ϕ) stripes are replaced with pixel sensors and there are thinner RF-aluminium foils with a thickness of ~ 250 μm , which help to have a better Interaction Point resolution.
- RICH1 possible improvements concerns mostly geometrical optics issues which converge on flat mirrors instead of spherical ones. As for the acquired signal it will be necessary to replace the multi-anode photomultipliers (MAPMT) with new photodetectors of higher granularity.
- The tracking stations will divided into one upstream detector (UT) replacing the TT module and three stations located downstream (after the magnet). The latter will be covered by a twelve-layer scintillating fibre tracker (SciFi) introduced already for Upgrade I. The key is again high granularity and so UT and the inner parts of T stations will be made with high-granularity silicon pixels.
- One new addition will be a TORCH detector whose purpose is to contribute to a better PID for kaons and protons with high precision time-of-flight measurements by internally reflected Cherenkov light. A time resolution of 70 ps per photon will allow the identification of kaons with momentum below 10 GeV/c, where currently they can only be selected by using the RICH in veto mode. Also low-momentum proton will be identified.
- The calorimeters will undergo to major changes. This topic is fundamental for the purposes of this thesis because the aim of the analysis was to study the performance of two of the substitute prototypes for ECAL. For this reason, further information about this topic are better discussed in the following sections. HCAL with its main purpose of hardware trigger will be removed in Run 5 removed and replaced with 1.7 m of iron which is an extra shielding for the muon chambers.

2.3 Motivations for a ECAL upgrade

The keys for the calorimeter improvement in Upgrade II are two: high performance both for energy and time resolution, and resistance to radiation damage.

With the higher luminosity obtained already after Run 3, a rapid degradation of the innermost modules of the calorimeter is expected. Furthermore, during Run 5 and 6 the greater number of showers at that luminosity condition would affect the energy resolution because of the unavoidable overlapping. Therefore it will be necessary to increase the granularity by scaling down the cell dimensions and introduce fast timing also to compensate the bigger combinatorial background coming from pile-up.

The former calorimeter was already described in Chapter 1 with its components details. Thus, in this section, there will be covered all the issues presented in trying to find out a substitute, what technologies are under investigation.

The radiation dose on the cells around the beam pipe is an important issue when it comes to HL-LHC. Several tests on the calorimeter modules were done, the last ones of 2015-2016 [6] showed that irradiating the nine 4x4 cm^2 cells of the inner module and measuring the dose on the surface, the performance loss would be around $40 - 50$ % after 10 kGy and around $60 - 70$% after 19 kGy . It is believed that the current ECAL would be able to endure until LS3 when the radiation dose will be $30 - 40$ kGy while the electronics will be changed. Of course for Upgrade II, when the dose will reach $1 - 2$ MGy, it would be required to change the modules each one or two years. A representation of the radiation impact on ECAL at full luminosity is shown in figure 2.3 [7] on the left where the coloured z axis represents the dose order of magnitude.

Timing information with a precision of few picoseconds will be required at high luminosity values in order to correctly associate a cluster to its primary vertex.

For what concerns the structure of the new ECAL, the three regions will become six in order to follow the radiation profile. The granularity of the cells in the inner regions will be increased and thus the Molière radius [14] will be reduced by employing different materials. Prototypes with a smaller cell size and a more resistant material such as tungsten (or tungsten alloy) are studied. For time measurements instead, silicon layers could be attached into the cell structure.

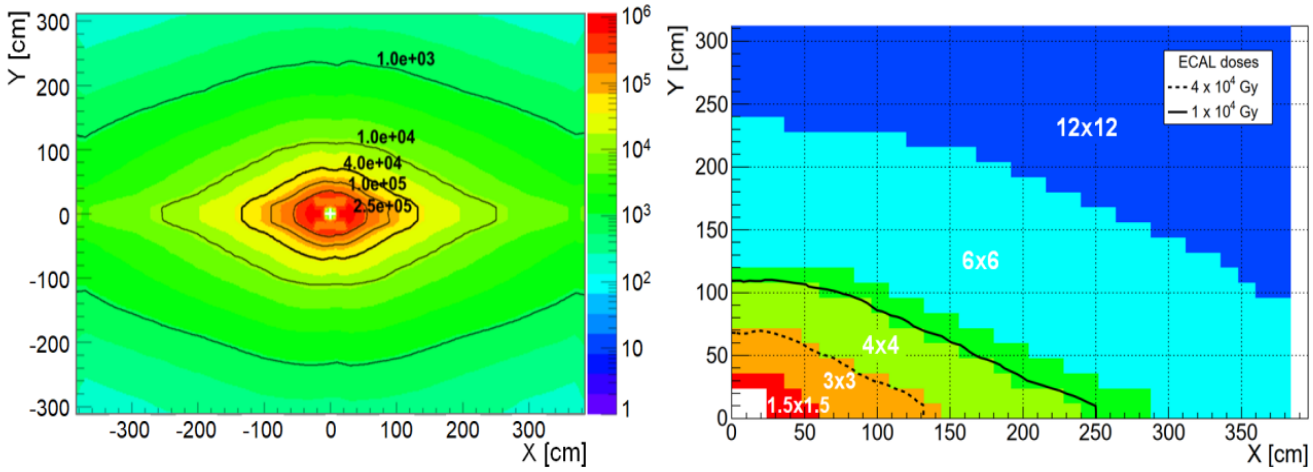

Figure 2.3: Expected accumulated radiation dose on ECAL after an integrated luminosity of 300 fb^{-1} (left). ECAL regions and cell sizes for Upgrade II with the SpaCal-Shashlik option (right). The dotted line delimits the current Shashlik radiation limit [7].

2.4 Calorimeter proposals

As already said, the radiation dose will be too high for the innermost modules to sustain. For the Shashlik technology the radiation limit is expected to be at 40 kGy which will be reached before LS3 [7]. The corresponding position in the ECAL module is represented by the dotted line on figure 2.3 on the right. Moving outward the dose will decrease and so other types of materials/technologies could be used. Starting with the most 'challenging' part, namely the inner modules, it was clear that crystal fibers were a valid option.

A technology with an absorber material and longitudinal crystal fibers running along the beam direction was proposed, hence the name Spaghetti Calorimeter. In figure 2.3 on the right, it is shown the radiation map of the future ECAL model, with the cell sizes with respect to the dose. Depending on that, different modules are chosen considering both performance and costs. Where the radiation is the most intense, there will be placed 32 1.5x1.5 cm^2 modules of SpaCal with tungsten absorber. Moving outwards, with a radiation between 40 and 200 kGy, there will be 144 3x3 cm^2 modules of SpaCal with lead absorber and Polystyrene fibers. Then the dose will be sufficiently low to allow the reutilization of Shashlik technology with 448, 1344 and 1344 modules respectively of 4x4 cm^2, 6x6 cm^2 and 12x12 cm^2. Table 2.4 summarizes all these modules characteristics, e.g. their resolution.

Alternatively, a 26-layer tungsten silicon sampling calorimeter which would replace all SpaCal/Shashlik modules is under investigation.

2.4.1 SpaCal prototypes

The SpaCal calorimeter prototype is composed by long fibers that act both as scintillator and as light transfer medium. Therefore WSL fibers, which would have been heavily affected by radiation, won't be required anymore.

Several tests have been done to find a suitable material, in particular Cerium-doped garnet crystals as $Y_3Al_5O_{12}$ (YAG) or $Gd_3Al_2Ga_3O_{12}$ (GAGG) seemed to have a good radiation hardness and time performance [12]. The absorber has to be a dense material such as tungsten or lead and its purpose

Region	Module type	Cell size [cm^2]	Segmentation [mm]/[X_0]	R_M [mm]	$\sigma_E/E = A/\sqrt{E} \oplus B$ A/B [%]
1	SpaCal W/GAGG	1.5×1.5	45+105/70+180	14.5	9.1 / 1.4
2	SpaCal Pb/PS	3.0×3.0	80+210/70+180	29.5	10.4 / 0.6
3	Shashlik	4.0×4.0	Continuous fibres	35.0	10.0 / 1.0
4	Shashlik	6.0×6.0	Continuous fibres	35.0	10.0 / 1.0
5	Shashlik	12.0×12.0	Continuous fibres	35.0	10.0 / 1.0
1-5	W-Si	10×10	26 layers	16.1	21.2 / 0.6

Figure 2.4: Characteristics of the modules in the SpaCal, Shashlik and W-Si options. The regions correspond to the differently coloured zones in Figure 2.3 (right). The parameters A and B have units of GeV$^{1/2}$ and GeV, respectively [7].

is to improve the granularity by keeping the shower dimension contained. Many GAGG crystal samples, which differs in composition and quality, were investigated with a ^{137}Cs radioactive source producing a light output from 27900 and 49500 photons/MeV (32140 for GFAG type [12]) and for time performance gamma excitations were performed obtaining light rise and decay time around 70 and 50 ps respectively. Polystirene fibers have been studied as well, with some great results from Kuraray (SCSF-78) with 10000 photons/MeV and a scintillation decay time of 2.8 ns [7].

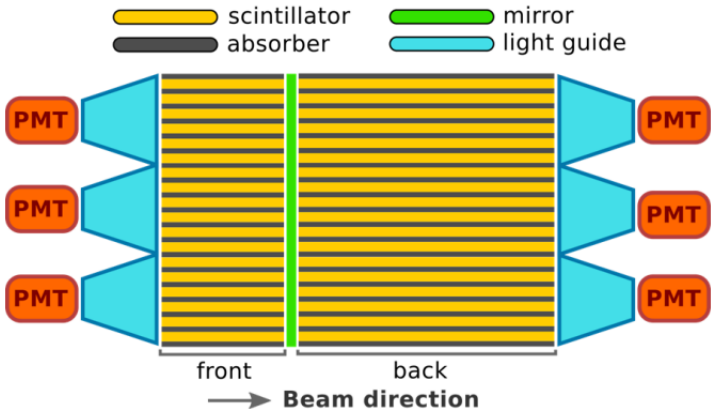

Figure 2.5: SpaCal module section schematization with scintillating fibers and PMT for readout [7].

The prototype structure is shown in picture 2.5: a striking feature of this prototype is the division into a front and back sections. It is possible to see the fibers running along the beam direction and transporting directly the light to the photodetectors, both on the front and the back section, which are read by a double readout system. This structure was chosen so that the shower maximum would be around the middle, the front section would suffer less from pile-up because the shower will be less developed while the back would use its timing information to help clusterisation over adjacent cells. A different option is to place a timing layer between these two sections, with MCP-PMT or a three-layer silicon detector.

In order to obtain a clear signal, it is necessary that the particle hits the fiber and not the absorber. However, if the prototype is perfectly aligned with the beam, only a few fibers would be crossed by the shower but the energy deposit would be great. On the other hand, if the prototype is tilted, more fibers would be hit with a smaller energy deposit. It is necessary then that one finds the good compromise.

Chapter 3

SpaCal test-beam and data analysis

The analysis presented here has been done on data taken during the test beam held in August 2021 at CERN on two different ECAL prototypes: SpaCal with W absorber and GAGG crystals (GFAG) and SpaCal with W absorber and Polystyrene fibres. The main purpose of the test beam is to establish the time performance of these prototypes, by using electron beams in the energy range from 20 to 100 GeV (20, 30, 50, 80, 100 GeV).

The experimental setup is shown in figure 3.1. The reference system of the test beam is defined by the z axis directed towards the electron beam, the y axis parallel and opposite to the gravity, and the x axis is chosen to form right-handed coordinates system. Two plates of plastic scintillation material allow to identify the electrons of the beam, triggering the signal acquisition on their coincidence. Two multichannel plates (MCP) are then set to give two timestamps - computed by a Constant Fraction Discriminator (CFD) - whose average was the initial reference time t_0. Then, to perform tracking there are three drift chambers, namely delay wire chambers (DWCs) as the signal is read out through a delay line, composed by two grids of wires dedicated to the x and y hit coordinate separately, filled by a mixture of gas Ar/Co_2. In this chapter the coordinates of the DWCs are indicated as (x_j,y_j,z_j), where the index $j = 0, 1, 2$ identifies the chamber from the one closer to the SpaCal prototype (0) to the one on the right (2). Lastly, there is the SpaCal prototype already described in the previous chapter enclosed in a dark box and free to rotate in the azimuthal and polar directions. Both studied prototypes are divided in front and back sections. As discussed in the next sections, the time performance have been evaluated for back and front separately, and for the average of the two. The electron beam with energies between 20 and 100 GeV is directed as in figure 3.1. All the modules hit by the beam lay on the xy plane orthogonal to the beam direction, namely the z axis. In this analysis the prototype was tilted to $3° + 3°$ in the azimuthal and polar directions.

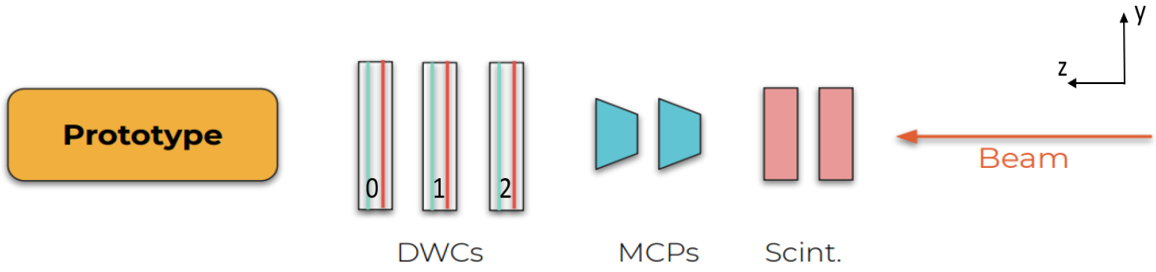

Figure 3.1: Layout of the experimental setup of August 2021 test beam. The electron beam is directed towards the z axis and impinges in order two scintillator pads, two multichannel plates, three delay wire chambers and lastly the prototype.

Data taken with both prototypes (SpaCal W/GAGG and SpaCal W/Polystyrene) are analysed to pursue two tasks: the first one is the study of the time resolution trend as function of the nominal beam energy; the second one is to measure the dependence of the time resolution with respect to the incident electron position on the SpaCal cell.

The analysis is performed with the software package ROOT [13].

3.1 SpaCal W/GAGG time resolution

First, it is assumed that the hit position in the DWC closer to the SpaCal prototype (x_0,y_0) is a proxy of the point where the beam enters the SpaCal cell. Hence it is necessary to remove the hits in the DWC associated to electrons that do not pass through the cell.

In order to do this, the respective signal intensity measured by the SpaCal prototype is paired with this DWC position obtaining the distribution shown in figure 3.2 for the beam at 20 GeV (left) and the beam at 100 GeV (right). The same procedure is repeated for the other beam energies.

It is possible to notice the different behaviour of the signal amplitude at different incident beam energies. This allowed to do a first estimation of the cell position in the (x_0, y_0) coordinates, locating it in a narrow interval with $x_0 \in [4, 12]$ mm and $y_0 \in [8, 16]$ mm.

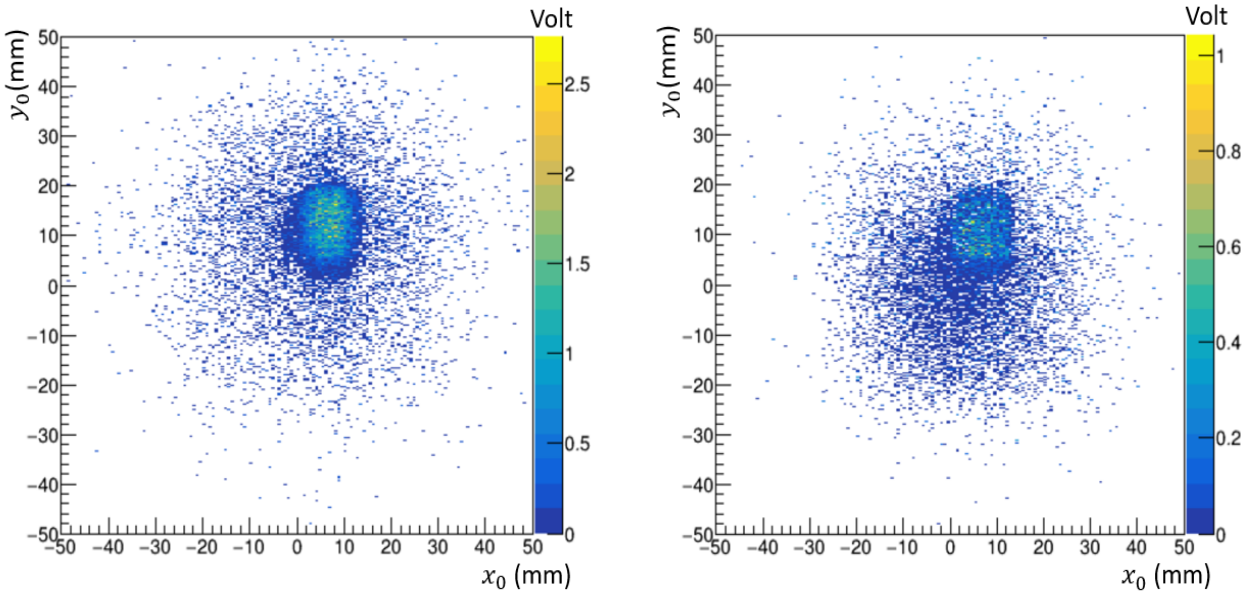

Figure 3.2: Signal amplitude on SpaCal front as a function of the time position in the closer delay chamber at 20 GeV (left) and 100 GeV (right).

To get an estimate of the SpaCal time resolution, initially the time resolution of the two MCPs, that are used to obtain the initial time t_0, has been measured. Event by event the difference between the second and the first MCP timestamps in coincidence ($t_2 - t_1$) is computed, obtaining a distribution which is fitted with a Gaussian curve. The resulting standard deviation is labelled as σ_{fit}.
Assuming that the resolution of both MCP is equal ($\sigma_{t_1} = \sigma_{t_2}$), the time resolution of one single MCP is $\sigma_{t_1} = \frac{\sigma_{fit}}{\sqrt{2}}$. The time t_0 is the average value between the MCPs timestamps ($t_0 = \frac{t_1+t_2}{2}$), therefore it is obtained that the resolution on t_0 is $\sigma_{MCP} = \frac{\sigma_{t_1}}{\sqrt{2}}$. A MCP resolution of $\sigma_{MCP} = \frac{\sigma_{fit}}{\sqrt{2}\sqrt{2}} = 13.6$ ps is obtained for electrons in the interval $x_0 \in [4, 10]$ mm and $y_0 \in [11, 17]$ mm.

Finally, the time resolution of the prototype is computed for front, back sections and also their average value in the following way. Event by event the average time of the MCPs, t_0, is subtracted from the time t read by the SpaCal prototype. A Gaussian fit is performed on the distribution obtained and thus the time resolution of the prototype is computed as $\sigma_{SpaCal} = \sqrt{\sigma_{fit}^2 - \sigma_{MCP}^2}$ where σ_{SpaCal} is the intrinsic resolution of the prototype, σ_{fit} is the standard deviation of the Gaussian fit and σ_{MCP} is the average time resolution of both MCPs computed before.

With these data, it is possible to obtain a SpaCal time resolution graph with as function of the beam energy, which is shown in figure 3.3.

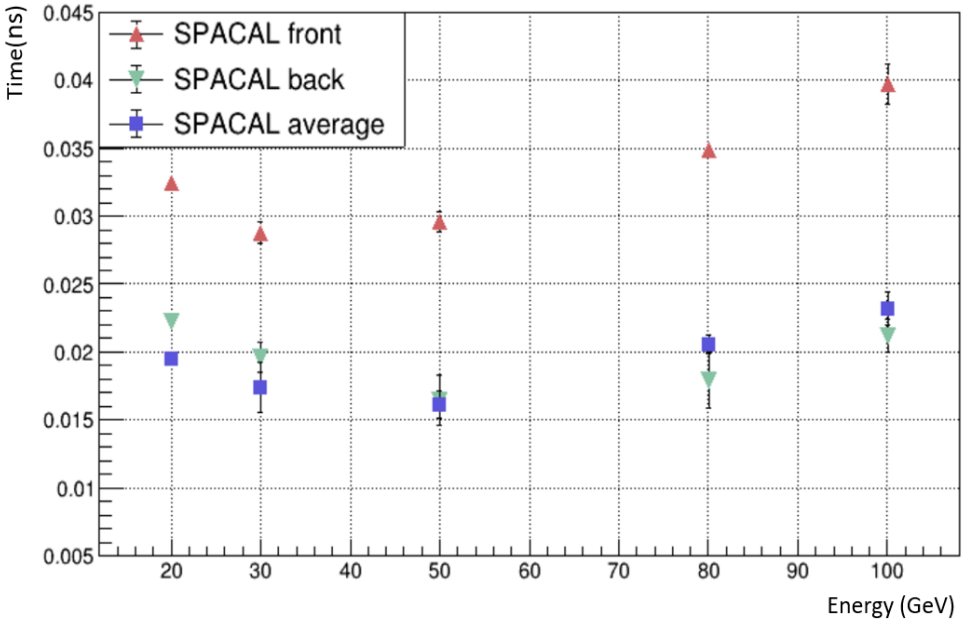

Figure 3.3: Time resolution of the SpaCal W/GAGG prototype as function of the beam energy.

The expected behaviour from reference SpaCal simulations is $\sigma \propto \frac{1}{\sqrt{E}}$ and it is more or less followed by data till 50 GeV. However, it appears that for 80 GeV and 100 GeV the time resolution is very different from what expected. Moreover, it can be noticed that the back section has a smaller ascent at high energies and in general has a resolution of $\sim$ 10 ps better than the front. This leads to a further investigation of the beam, and in particular its position on the three DWCs in order to remove possible signals produced by multiple scattering or by a bad beam collimation.

From the analysis of the signal position in two of the three chambers (figure 3.4), it is possible to notice that the linear dependence is not fully respected. Moreover, a halo is visible around the line in the central spatial position. In fact, if the chamber were placed perfectly on a plane perpendicular to the beam direction, the trend would be a bisector of the first quadrant.

Hence, two different requests were done to remove the beam halo:

- a "band cut" on the x and y coordinate of the DWCs was performed, where it is chosen a linear belt parallel to $y_j = x_j$ around the data and all the points outside are eliminated;
- a "tracking cut", by fitting the DWCs coordinates into a straight line and minimising the squared distance.

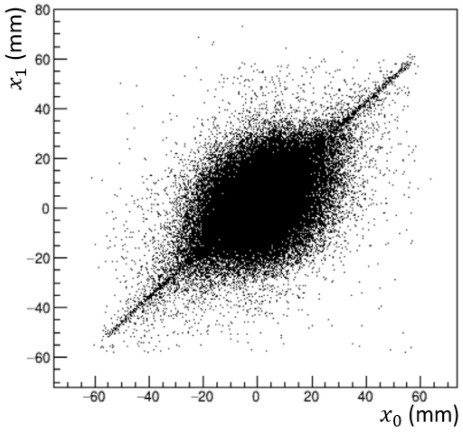

Figure 3.4: Signal position of two DWCs (x_0, x_1) without amplitude cut on MCPs.

The "band cut" is performed by removing all the points which are not contained in these intervals (in mm): $0 \leq x_0 - x_1 \leq 6$, $2 \leq x_0 - x_2 \leq 10$, $-3 \leq y_0 - y_1 \leq 6$ and $-1 \leq y_0 - y_2 \leq 10$, where x_0, x_1, x_2 and y_0, y_1 and y_2 are respectively the x and y positions on the first, second and third DWC from left to right. A better linear trend is obtained and repeating the time resolution computations it is possible to see a higher resolution at every energies, with respect to the previous result without cut. In particular, the average resolution at 100 GeV seems to improve more. The results are shown in the figures 3.5 and 3.6.

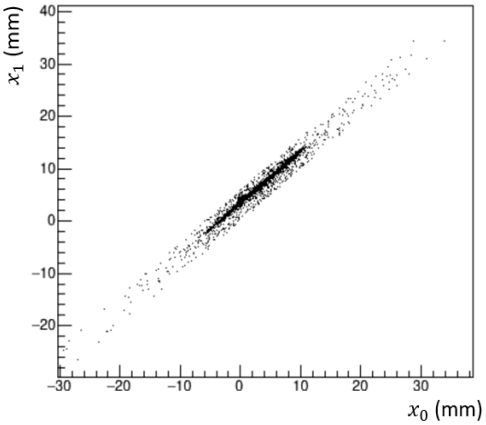

Figure 3.5: Signal position on the first and second DWC with band cut.

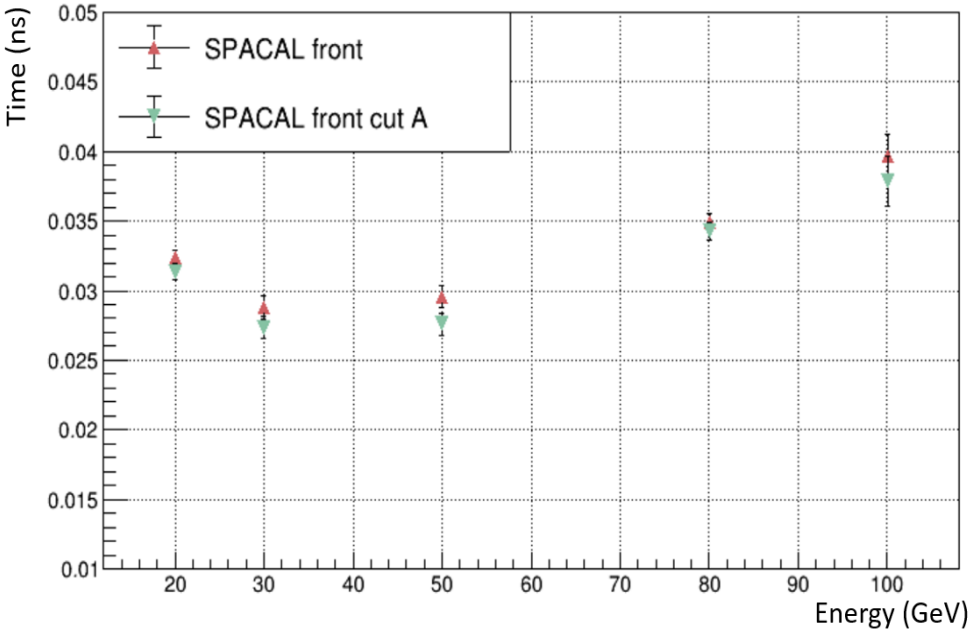

Figure 3.6: Time resolution as function of the average SpaCal energy with and without band cut.

The track reconstruction is performed by computing the distance between every point of the three delay wire chambers and a 3-dimensional line which connects all three points on the DWCs at their respective z coordinate. The DWC positions are fixed on the z axis at z_0, z_1 and z_2. The point coordinate on the DWC is $\vec{x}_{ij} = (x_{ij}, y_{ij}, z_{ij})$ where i is a single point on a DWC and $j = 0, 1, 2$ are the three chambers, and so the normalized distance between these points and the 3D line is $d_{ij} = \frac{\vec{x}_{ij} - \vec{x}_{ij,line}}{\|\vec{x}_{ij} - \vec{x}_{ij,line}\|}$.
These distances are then minimised with the Ordinary Least Squares method. The minimised quantity S defined as $S = \sum_{j=1}^{3} \sum_{i=1}^{N} (d_{ij})^2$ is then plotted, see figure 3.7 (b), to determine a threshold. Points with a S value greater than 0.2 are removed.

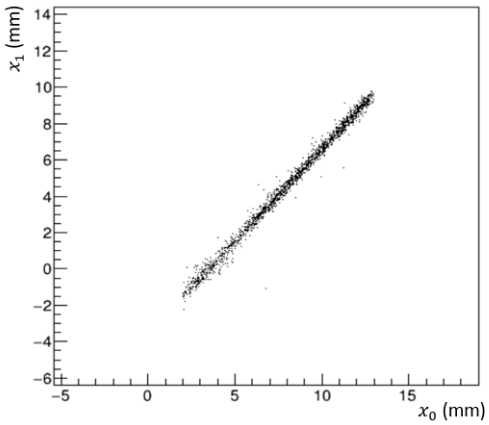

(a) Signal position of the first and the second DWC with tracking cut.

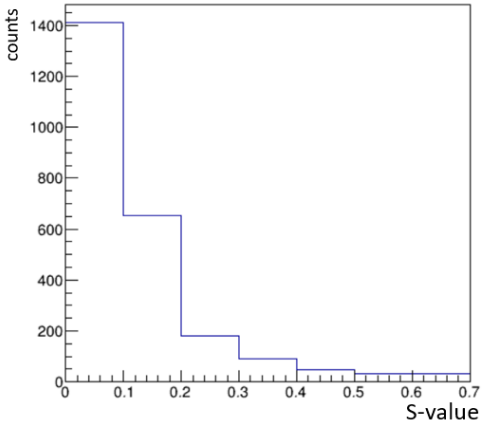

(b) S-value distribution for tracking cut.

Figure 3.7: Signal position on DWC and relative minimisation with tracking cut.

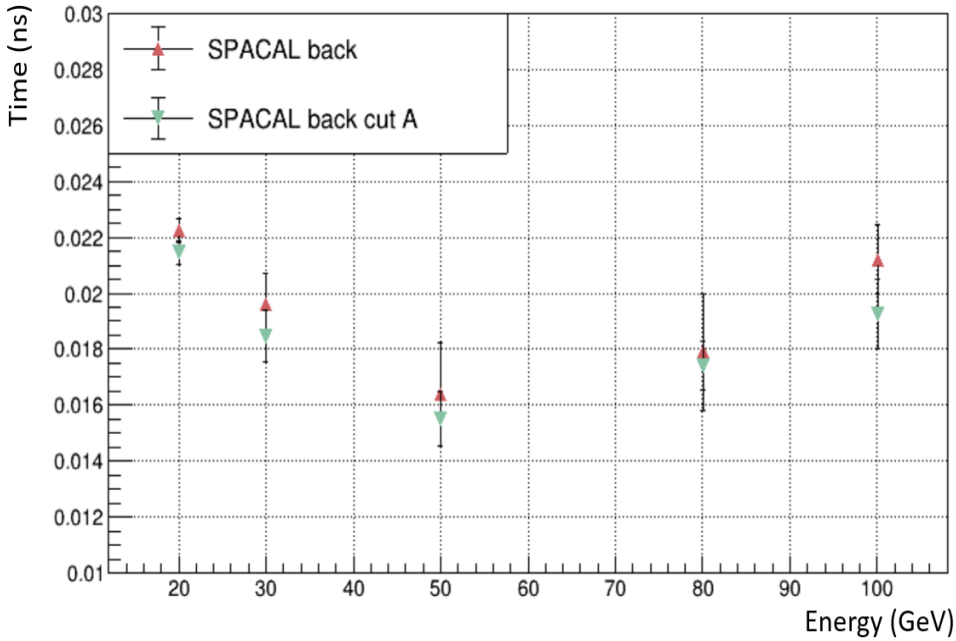

Figure 3.8: Time resolution curve as function of energy of SpaCal average with and without tracking cut.

Data selected with the tracking requirement follows the expected trend until 50 GeV, it shows a better time resolution with respect to the not selected data, especially at 100 GeV.

However, even after performing this type of selection on data obtaining a better resolution (figure 3.7 (a)), it appears that this method is inadequate to improve significantly the time resolution measurement at higher energies. This behaviour can be attributed to the beam characteristics and it should be investigated more in the future.

3.1.1 Cell division

Another important objective of this analysis is to look for the time resolution as a function of the part of the prototype cell hit by the beam. In fact, the test beam was performed with only one cell (there should be 9 in the inner region of ECAL) and so the behaviour in the zone adjacent at other cells has be studied. In fact possible edge effects could have an impact on the time resolution between two cells. In order to proceed, a position interval in the DWC closer to the SpaCal prototype is chosen, bigger then the one used in the previous computation since the aim of the analysis is to study edge effects.

The intervals are then $x_0 \in [2, 13]$ mm and $y_0 \in [4, 18]$ mm. The x_0 interval is noticeably lower then 15 mm - which is the cell dimension - because it was impossible to unambiguously identify a unique interval that locates the cell for all the energies.

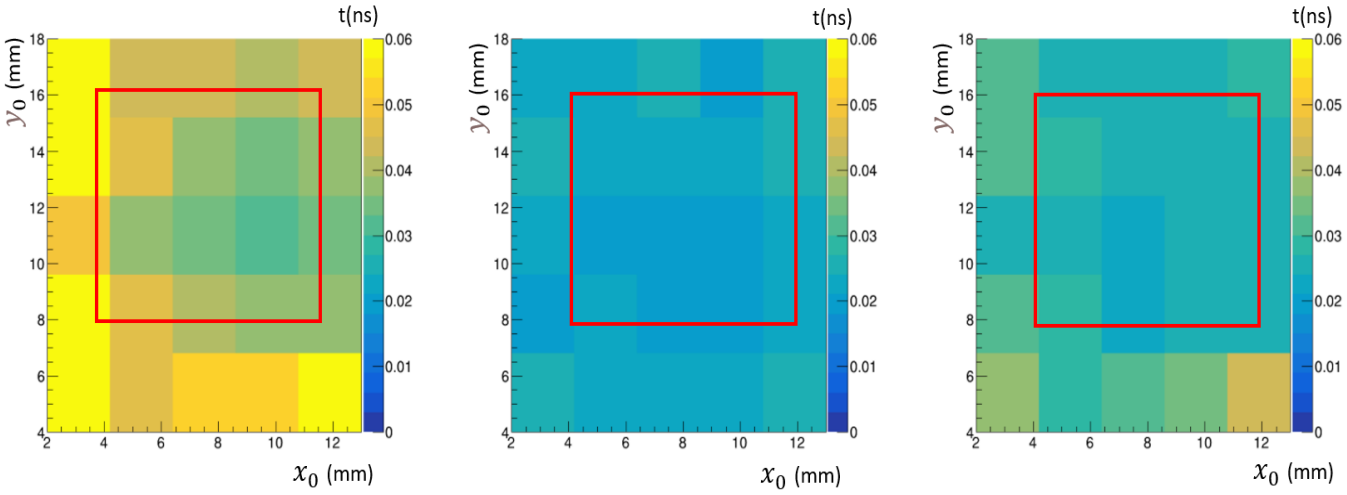

Figure 3.9: Time resolution map per cell division 5x5 at beam energy 80 GeV of SpaCal front, back and average sections without any requirement.

The Spacal cell has been divided in 5×5 subcells. Every subcell was analyzed as in figure 3.9 for front, back and average SpaCal at every energies with and without band and tracking requirements. What can be easily noticed is that the (x_0, y_0) position cut done in the previous analysis, indicated with the red line, does not perfectly match the best resolution zone.

The front section of the cell has a worse time resolution in the left and lower region, while for the back section the time resolution is more uniform.

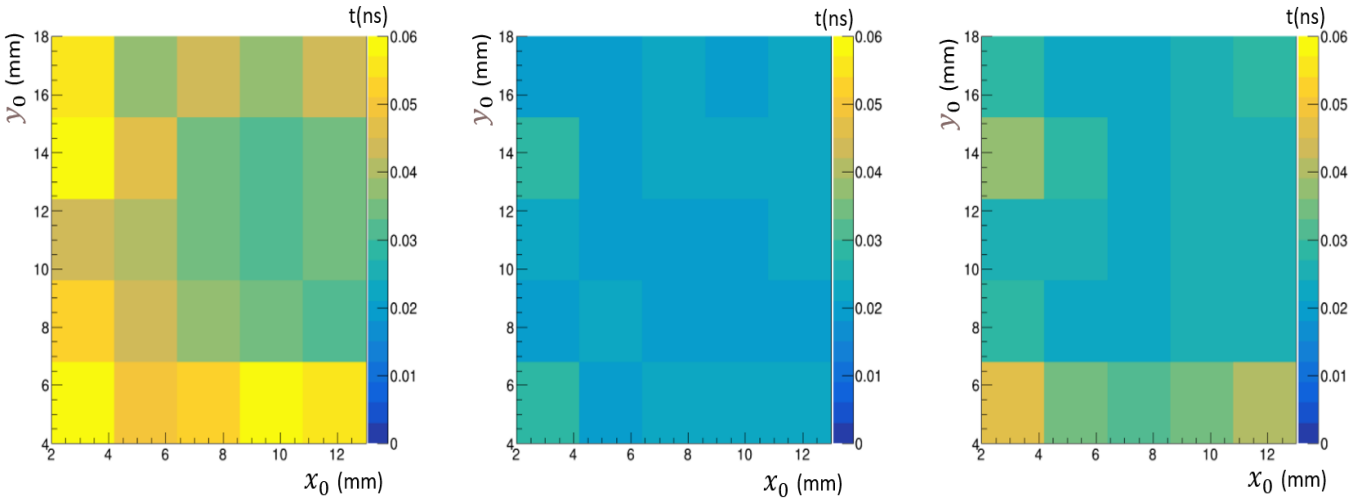

Figure 3.10: Time resolution map per cell division 5x5 at beam energy 80 GeV of SpaCal front and back sections and average with tracking cut.

Same considerations can be done for figure 3.10 where the effect of the tracking requirement can be seen with respect of figure 3.9 which shows the same graph without any requests.

Lastly, on figure 3.11 the time resolution of the front section is compared at three different energies 100 GeV, 50 GeV and 20 GeV. The right figure exhibits a higher time resolution than the central one, as expected (worse resolution at lower energy according to $E^{-1/2}$). On the other hand the left figure shows the time resolution at 100 GeV is noticeably high. Once again the previous position used for the time resolution computing is outlined with a red square.

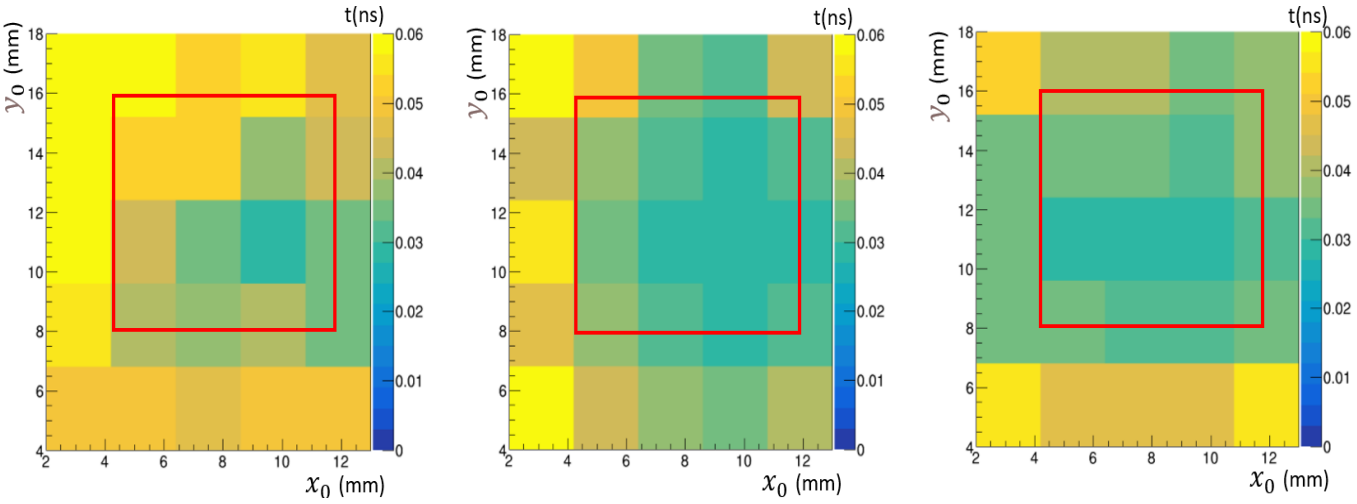

Figure 3.11: Time resolution map per cell division 5x5 of SpaCal front section with band requirement at beam energy of 100 GeV, 50 GeV and 20 GeV from left to right.

3.2 SpaCal W/Polystyrene time resolution

The same analysis is done also with another prototype, SpaCal with tungsten absorber and polystyrene fibers.

To identify the cell position of this prototype in the (x_0,y_0) plane, the signal amplitude distribution is analyzed, choosing the interval with $x_0 \in [4, 12]$ mm and $y_0 \in [8, 15]$ mm. The MCP resolution is then computed obtaining a value of 14 ps.
Time resolution of the prototype is obtained by $\sigma_{SpaCal} = \sqrt{\sigma^2_{fit} - \sigma^2_{MCP}}$ and compared among front, back sections and the average in figure 3.12 as function of the beam energy.

The front section has a worse resolution than the back one, as seen in SpaCal W/GAGG ($\sim$ 60 ps). The expected trend of $\sigma \propto E^{-1/2}$ is more or less followed except for the 100 GeV point (figure 3.12 (b).

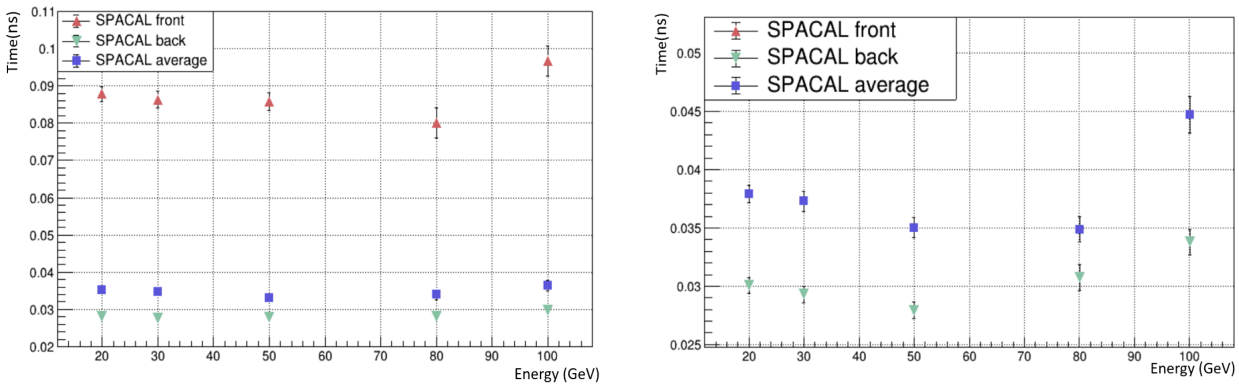

(a) Back, front and average sections resolution.

(b) Back resolution zoom in.

Figure 3.12: Time resolution of the SpaCal W/Polystyrene prototype as function of the beam energy.

As for the SpaCal W/GAGG prototype, a band and a tracking requirements are applied. The band intervals are (in mm): $2 \leq x_0 - x_1 \leq 4$, $4 \leq x_0 - x_2 \leq 8$, $-3 \leq y_0 - y_1 \leq 2$ and $1 \leq y_0 - y_2 \leq 4$, where x_0, x_1, x_2 and y_0, y_1 and y_2 are respectively the x and y positions on the first, second and third DWC from left to right, obtaining the signal position distributions shown in figure 3.13. The effect of the tracking requirement on the beam is very clear in figure 3.13 (c) where all events with an S-value more than 0.2 are eliminated.

By comparing the resolution with or without selection requirements, the graphs in figure 3.14 is

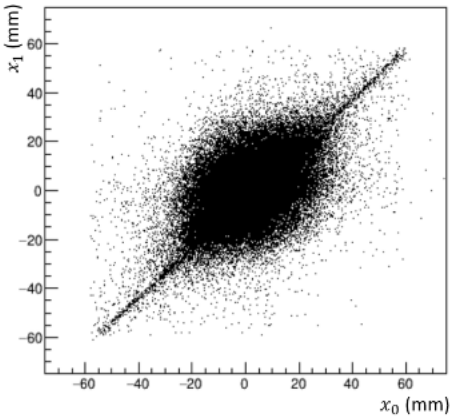

(a) Signal position of two DWCs (x_0, x_1) without amplitude cut on MCPs.

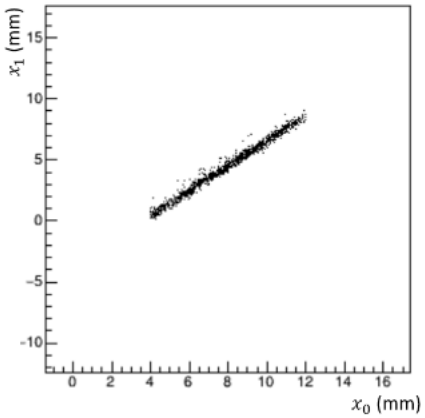

(b) Signal position on the first and second DWC with band cut.

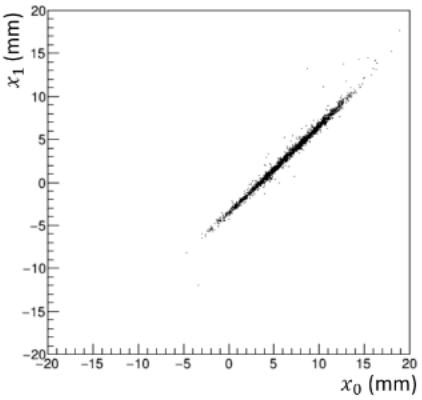

(c) Signal position of the first and the second DWC with tracking cut.

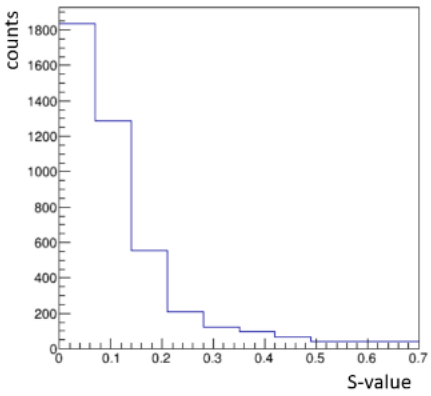

(d) S-value distribution for tracking cut.

Figure 3.13: Signal position of two DWCs (x_0, x_1) without amplitude requirement on MCPs (up left), with band requirement (up right), with tracking requirement (bottom left) and relative S-value distribution (bottom right).

obtained where it is possible to see that both requirements contribute significantly to the resolution increasing.

3.2.1 Cell division

For the SpaCal with polystyrene prototype it has been more difficult to find the right (x_0, y_0) interval of the cell position, as it is possible to see in figure 3.15. A larger interval ($x_0 \in [2, 13]$ mm and $y_0 \in [4, 18]$ mm) is then chosen, in order to investigate possible edge effects at the cell border.

After, this interval is split into 5×5 sub-cells and the signal time resolutions corresponding to the sub-cell appear in figure 3.16.

The band and the tracking requirements are performed also on the analysis of data of this prototype. The tracking requirement appears to improve the resolution. The front section seems to have a better resolution in the central region, which almost corresponds to the interval chosen for the analysis in the previous section, outlined with a red square on figure 3.16. In this figure there are the time resolution maps for front, back and average sections at 20 GeV with and without tracking requirements.

Once again, the back section is the most homogeneous one.

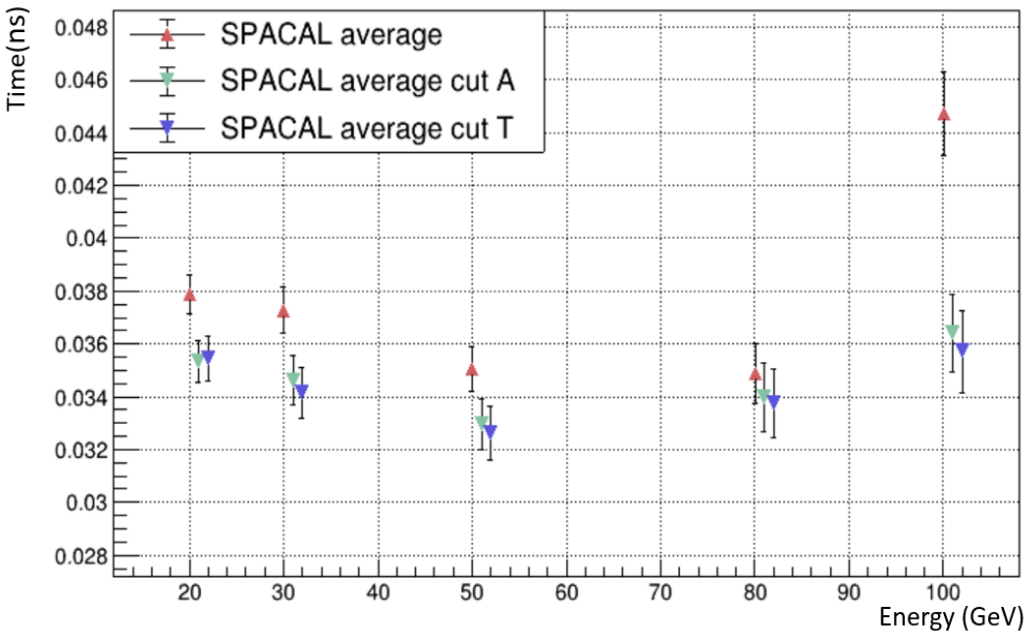

Figure 3.14: Time resolution curve as function of energy of SpaCal average with band and tracking requirement and without. The x coordinate is slightly translated for points corresponding to band and tracking requirement in order to see non overlapping error bars.

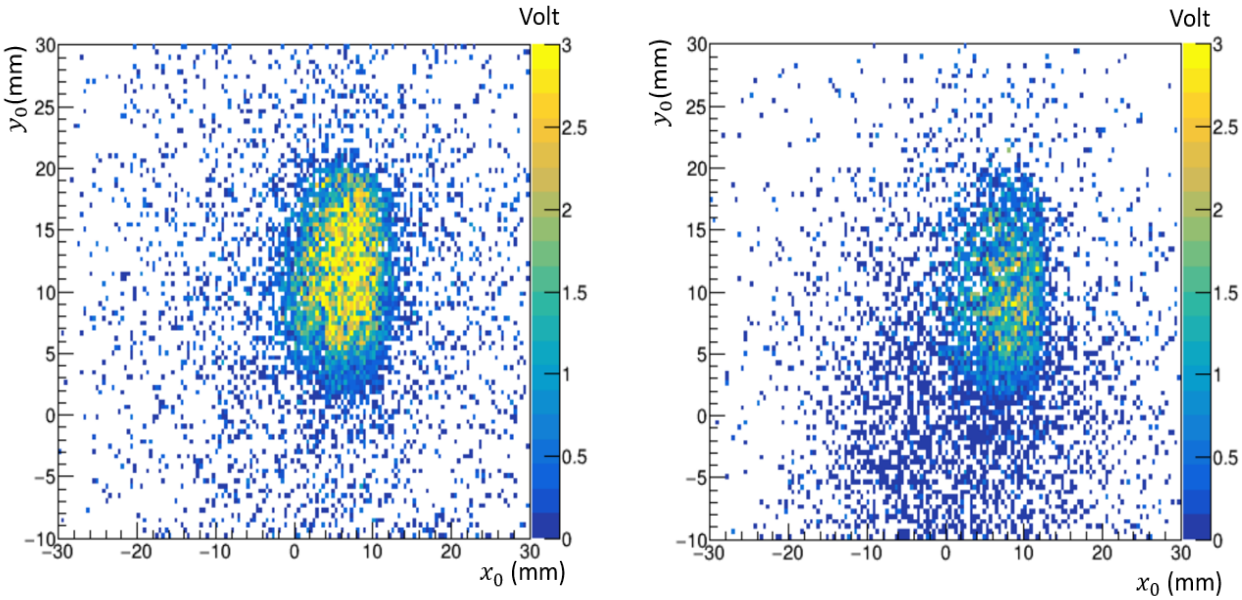

Figure 3.15: Signal amplitude on SpaCal front as a function of the time position in the closer delay chamber at 20 GeV (left) and 80 GeV (right).

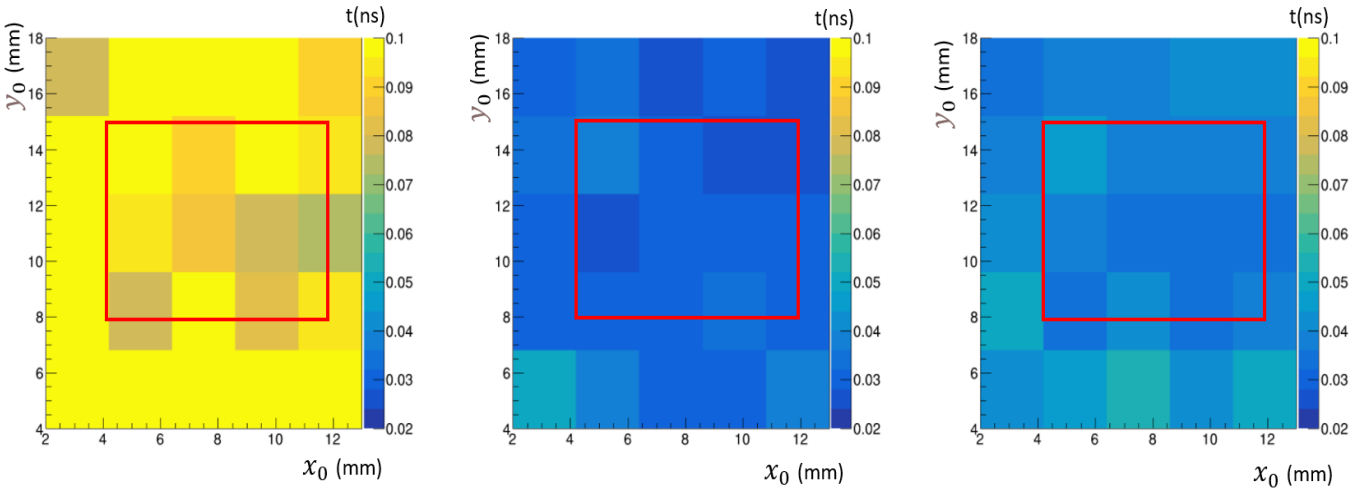

Figure 3.16: Time resolution map per cell division 5x5 at beam energy 20 GeV of SpaCal front, back and average sections without any cut. The red square outlines the region of the previous position interval.

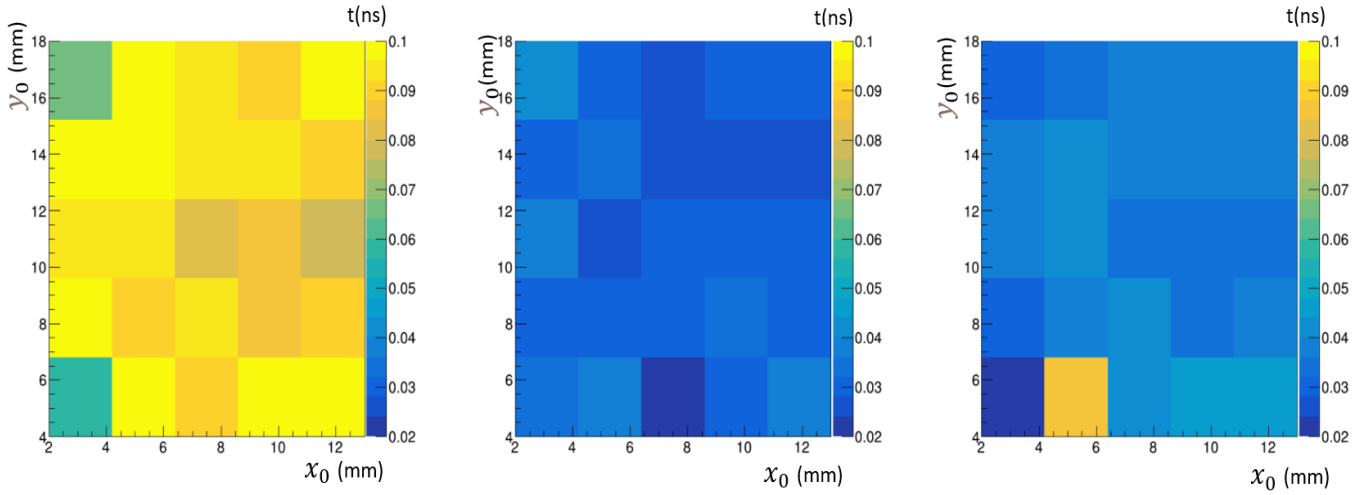

Figure 3.17: Time resolution map per cell division 5x5 at beam energy 20 GeV of SpaCal front, back and average sections with tracking requirement.

Chapter 4

Conclusions

In this thesis, data taken during the test-beam campaign in August 2021 at SPS on two different ECAL prototypes have been analysed. Their time performance, and therefore the feasibility for these prototypes to be used in the LHCb Upgrade II, is studied.

For the purposes of this analysis, it was briefly explained what the HL-LHC program is and which are the consequences on the LHCb detector, specifically on the calorimeter system, with the new idea of removing HCAL and completely renovating the actual ECAL Shashlik technology. Moreover, the addition of precision time measurements, in order to better associate the ECAL clusters with the corresponding proton-proton interaction, has been discussed.

For both prototypes, SpaCal W/GAGG and SpaCal W/Polystyrene, the time performance of a single module cell of 1.5x1.5 cm^2 has been studied using an electron beam with nominal energy from 20 to 100 GeV.

On one side it was desirable to obtain a time resolution as a function of the electron energy that follows the relation $1/\sqrt{E}$, as obtained from simulations. On the other side, possible edge effects at the cell border were investigated, analysing time resolution in smaller cell subdivisions.

For the SpaCal W/GAGG prototype, it was possible to identify the expected trend for the time resolution apart from 80 and 100 GeV where the resolution worsens. Two different techniques have been applied to remove the beam halo and improve the time resolution measurement, namely "band" and "tracking" requirements. However, the behaviour is not the expected one. The time resolutions obtained in this way are on average around $16 - 20$ ps. The same results were obtained in the cell division study, where it was possible to identify better time resolution in the central region of the cell.

As for SpaCal W/Polystyrene, the same analysis has been repeated. The time resolutions for this prototype are on average around 32-36 ps. The cell division analysis was also done resulting in a overall uniform resolution for the back section of the prototype and a non-homogeneous one for the front section.

The time resolutions obtained in the test beam are compatible with those required by the HL-LHC environment, that should be around 20 ps. The SpaCal W/GAGG prototype has a better time resolution with respect to the SpaCal W/Polystyrene. However the time resolution as a function of the particle energy does not respect the expected behaviour due to beam characteristics like the halo contamination. For this reason further investigations are needed, and an improved setup for the future test beams should be defined.

Bibliography

[1] L. Evans and P. Bryant, *LHC Machine*, JINST 3 (2008) S08001.

[2] LHCb, A. A. Alves, Jr. et al., *The LHCb Detector at the LHC*, JINST 3 (2008) S08005.

[3] S. Barsuk, *The shashlik electro-magnetic calorimeter for the LHCb experiment*, CERN-LHCb-PROC-2004-006.

[4] LHCb Calorimeters, *Technical Design Report*, CERN/LHCC/2000-0036.

[5] LHCb collaboration, *Physics case for an LHCb Upgrade II — Opportunities in flavour physics, and beyond, in the HL-LHC era*, arXiv:1808.08865.

[6] Yu. Guz, *The LHCb Calorimeter system: design, performance and upgrade*, 2017, JINST 12 C07024.

[7] T. LHCb Collaboration, *Framework TDR for the LHCb upgrade II*, CERN/LHCC 2021-yyy, 2021.

[8] T. LHCb Collaboration, *Framework TDR for the LHCb upgrade*, CERN/LHCC 2014-001, 2014.

[9] Karol Hennessy, *LHCb VELO upgrade*, Nucl. Instrum. Meth. A845 (2017) 0168-9002.

[10] F. Follin, D. Jacquet, *Implementation and experience with luminosity levelling with offset beam*, 10.5170/CERN-2014-004.183 (2014), arXiv:1410.3667.

[11] L. Martinazzoli, *Crystal Fibers for the LHCb Calorimeter Upgrade*, in IEEE Transactions on Nuclear Science, vol. 67, no. 6, pp. 1003-1008, June 2020, doi: 10.1109/TNS.2020.2975570.

[12] L. Martinazzoli, N. Kratochwil, S. Gundacker, and E. Auffray, *Scintillation properties and timing performance of state-of-the-art gd3al2ga3o12 single crystals*, Nuclear Instruments and Methods in Physics Research Section A: Accelerators, Spectrometers, Detectors and Associated Equipment 1000 (2021) 165231.

[13] Rene Brun and Fons Rademakers, *ROOT - An Object Oriented Data Analysis Framework*, Proceedings AIHENP'96 Workshop, Lausanne, Sep. 1996, Nucl. Inst. & Meth. in Phys. Res. A 389 (1997) 81-86. See also "ROOT" [software], Release v6.18/04, 11/09/2019.

[14] P.A. Zyla et al. (Particle Data Group), Prog. Theor. Exp. Phys. 2020, 083C01 (2020).